Tuning the electronic band gap of Cu₂O via transition metal doping for improved photovoltaic applications

Aleksandar Živković ⬭, Alberto Roldan, and Nora H. de Leeuw*

Cardiff University, School of Chemistry, Main Building Park Place, Cardiff CF10 3AT, United Kingdom

Cu₂O is a widely known *p*-type semiconductor with a band-gap value suitable for photovoltaic applications. However, due to its parity-forbidden nature of the first interband transition and high carrier recombination currents, Cu₂O has failed to reach commercial application. Hybrid density functional theory has been used to study the effect of transition metal dopants on the electronic and optical properties of Cu₂O. Substitutional transition metal dopants, incorporated on the copper site, allow band-gap tunability by creating a range of defect states in the electronic structure, from shallow levels to deep intermediate bands. The preferred position of the dopants is in the vicinity of copper vacancies, which are naturally found in Cu₂O and are responsible for its *p*-type conductivity. Impurity levels created via extrinsic transition metal dopants increase substantially the capacity of Cu₂O to absorb light, reaching values close to 10%. First row transition metal dopants thus show potential for considerable improvement of the overall photovoltaic performance of Cu₂O.

I. INTRODUCTION

Since solar energy is an easy to obtain and an inexhaustible source, sunlight converters are increasingly attracting scientific attention. As a result, an intensive search is being carried out for new low-cost materials for the fabrication of solar conversion devices [1]. Despite the apparent efficiency of perovskites in solar cell applications [2–4], the search for oxide absorbers remains highly relevant, mostly due to their stability under atmospheric conditions, abundancy, and nontoxicity. Photoactive oxides are environmentally friendly and cost-effective, making them ideal for large-scale photovoltaic deployment [5].

Cuprous oxide [Cu₂O, copper (I) oxide] is a promising alternative to traditional thin-film photovoltaic materials (CIGS, CdTe, *α*-Si, etc.) because of its low materials cost, abundance of its component elements, and uniquely straightforward manufacturing process [6,7]. It has recently received renewed interest as a photovoltaic and photocatalytic material, mainly due to its favorable band-gap energy of 2.17 eV, high hole mobility, and favorable band edge positions [8–11]. However, the foremost optical transition at the band-gap energy is parity-forbidden, leading to a weak absorption onset, which limits the efficiency of Cu₂O as a thin-film absorber [12,13]. Low output conversion efficiencies have also been attributed to high carrier recombination rates and intrinsic trap states limiting the final photocurrent [14–16].

Controlling the presence of dopants in oxides provides an important mechanism to tune and alter the optoelectronic properties of a given compound [17]. Transition metal (TM) impurities, introduced in semiconducting compounds, are able to create a range of energy levels in the band gap [18]. Doping

has already been shown to provide a way of improving the photostability of Cu₂O, circumventing complicated fabrication processes such as coating, integration with other materials and use of co-catalysts [19].

Some key aspects of intrinsic defects have already been identified in the literature. The *p*-type conductivity of Cu₂O was found to originate from small amounts of Cu vacancies (V_Cu), with a formation energy depending on the oxygen partial pressure and temperature condition of synthesis [20–22]. Theoretical studies confirmed the most favorable polaronic defects in Cu₂O to be simple (V_Cu) and split vacancies (V_Cu^split), demonstrating the need to go beyond local and semilocal theoretical approximations to capture the essential nature of those processes accurately [23–25].

Experimentally, Cu₂O has been doped with many extrinsic elements, e.g., N [26,27], Cr [28], Fe [28,29], Au [28], Mg [30], Co [31,32], Mn [33], and Zn [17,19,34] mostly in the form of thin films and bulk samples. A pronounced difficulty is to achieve effective cation incorporation in the Cu₂O matrix and at the same time avoid the formation of local impurity clusters or dopant-based oxides [19].

Several theoretical papers have treated the possibility of tuning the bang gap of Cu₂O with cation doping. Martinez-Ruiz *et al.* [1] have used density functional theory (DFT) calculations to study copper (I) oxide doped with Ni, Zn, and Ag. Their results indicated a reduction of the band gap with Ag doping, whilst Ni and Zn favor *p*-type and *n*-type semiconducting behavior, respectively. Nolan and Elliott [24] have used DFT-GGA to explore the possibility of tuning the transparency of Cu₂O through cation doping (including Ba, Sn, Ti, Cr, V, amongst many others). A decrease of the band gap with transition metal dopants was observed, while alkaline Earth elements favored an increase of the initial value. Isseroff and Carter [14] have used a hybrid-DFT approach to study the effect of Li, Mg, Mn, and Zn dopants on vacancy

---

*Corresponding author: deleeuwn@cardiff.ac.uk

formation energies, electronic structure, and photoconductivity of Cu_2O. A thermodynamic preference to forming defect pairs was observed, including dopant rearrangement into a fourfold coordination. The proper usage of well-converged k-point meshes was elucidated to have a significant impact on hybrid-DFT results, in contrast to previous theoretical results.

Despite the significant effort invested into exploring the conventional properties of doped Cu_2O, relatively less effort has been devoted to study the impact of extrinsic dopants on the photovoltaic properties of Cu_2O. Moreover, theoretical investigations performed at the general gradient approximation level often lack completeness in the description of oxide electronic properties [35]. In this study, the effect of first row transition metal (FRTM) dopants on the overall photovoltaic absorption potential of Cu_2O is explored, using a systematic hybrid-DFT approach. The effect of dopants on the electronic structure is examined, together with their formation energies, charge distribution, and influence on the optical response. In addition, a selection metric is employed to assess the limiting power conversion efficiency of doped Cu_2O.

II. COMPUTATIONAL DETAILS

The theoretical results presented here were based on spin polarized DFT-based calculations performed with the Vienna *ab initio* simulation package [36]. The interactions between core and valence electrons were represented using the projector augmented wave (PAW) method [37].

The general gradient approximation (GGA) [38] exchange-correlation (XC) functional with the Perdew-Burke-Ernzerhof (PBE) parametrization was employed for DFT + U within the formalism of Dudarev *et al* [39]. The values for the effective Hubbard parameter (U_{eff}) were taken from parameter-free self-consistent calculations, yielding accurate electronic

properties for transition metal oxides [40–42]. For the hybrid-DFT calculations, the HSE06 XC functional was used, which incorporates 25% of the nonlocal exact Hartree-Fock (HF) exchange and a screening parameter of $0.2\,Å^{-1}$ [43–45]. The hybrid functional approach demonstrated accurate descriptions of various oxide semiconductors, including Cu_2O [10,11]. The method of Gajdoš *et al.* was used to obtain the real and imaginary parts of dielectric functions [46], from which the absorption coefficient was derived. Long distance dispersion corrections were included using the D3 approach of Grimme *et al.* [47]. The plane wave expansion cutoff was set to 500 eV and the force convergence criterion to cell relaxation was 0.01 eV/Å.

Cu_2O crystallizes in a high-symmetry cubic structure containing six atoms in the unit cell arranged in the cuprite structure. The initial computed Kohn-Sham band gap (with the HSE06 functional) at the Γ point is 2.052 eV (see Fig. 1), in good agreement with the experimental value of $2.1-2.4$ eV [48]. Defects were modelled in a 48-atom ($2 \times 2 \times 2$) supercell where one Cu atom was replaced with a FRTM dopant giving a concentration of 3.125%, which is accessible well within the experimental regime [49,50]. The starting supercell lattice constant was 8.461 Å, obtained from DFT + U calculations on the stoichiometric unit cell. A Monkhorst-Pack [51] k mesh of $3 \times 3 \times 3$ was employed to ensure total energy convergence up to 1 meV/atom.

DFT + U, which has been shown to accurately reproduce the structural parameters of the stoichiometric unit cell, was used to relax the doped Cu_2O structure (including atomic position and volume optimization), whilst hybrid-DFT permitted an accurate electronic structure at affordable computational cost [52]. Based on the band structure, the optical absorption spectra were obtained by calculations from the real and imaginary parts of the dielectric function within the
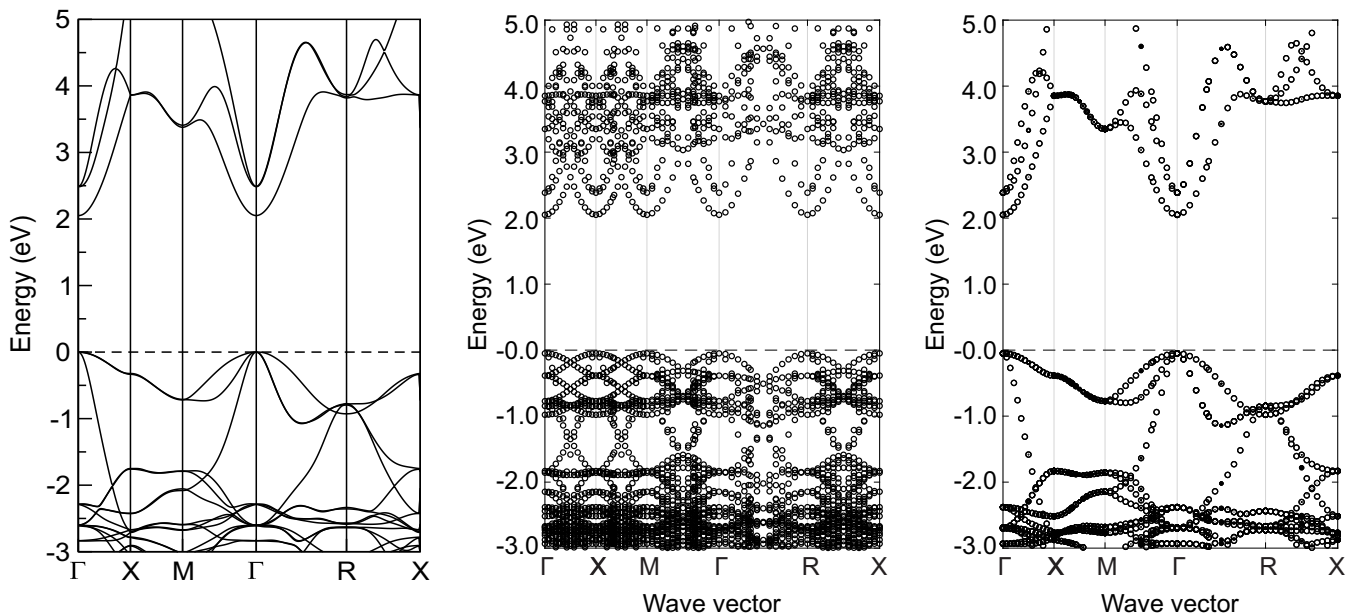

FIG. 1. Calculated band structure for a Cu_2O unit cell (left) together with the unfolded band structure of a Cu_2O $2 \times 2 \times 2$ supercell (middle). After unfolding has been performed, the effective band structure in a primitive representation has been obtained (right), which matches the initial band structure accurately.

TABLE I. Enthalpies of formation (eV/formula unit) for Cu$_2$O, Cu$_4$O$_3$, and CuO.

	$\Delta H_{\mathrm{f}}(\mathrm{Cu_2O})$	$\Delta H_{\mathrm{f}}(\mathrm{Cu_4O_3})$	$\Delta H_{\mathrm{f}}(\mathrm{CuO})$
DFT + U	−1.72	−4.99	−1.62
HSE06	−1.66	−4.92	−1.57
Experiment	−1.75 [68]	−	−1.59 [68]

independent particle approximation. Since DFT and DFT + U fail to accurately model the formation energies of defects in Cu$_2$O [23,52], defect formation energies were calculated using a single point calculation with hybrid-DFT.

The phase stability diagram of Cu$_2$O for a range of accessible chemical potentials was computed using the CPLAP (Chemical Potential Limits Analysis Program) [53], taking into account its limiting competing phases. All reference enthalpies and elemental energies were calculated keeping the hybrid exchange-correlation functional consistent to ensure transferability of results. The extent of defect charge distribution was studied using the Bader scheme as implemented in the Henkelman code [54–56]. All inequivalent dopant configurations for site substitutions in the supercell approach were generated using the Site-Occupation Disorder package [57]. Graphical drawings were produced using VESTA [58] and band structure unfolding was performed using the FOLD2BLOCH software [59,60]. Excitonic and spin-orbit coupling effects were not taken into account.

Phase stability

The formation enthalpy of a neutral defect $\Delta H_f(D)$ is defined as

$$\Delta H_{\mathrm{f}}(D) = E_{\mathrm{tot}}(D) - E_{\mathrm{tot}}(H) + \sum_i n_i \mu_i, \quad (1)$$

where $E_{\mathrm{tot}}(D)$ and $E_{\mathrm{tot}}(H)$ are the total energies of the system with and without the defect (D), respectively. The value n_i represents the number of atoms of element i that are removed from the system to form a defective structure (a negative value denotes addition of atoms) and μ_i is the chemical potential of element i. The chemical potential can be written as $\mu_i = \mu_i^{\mathrm{elem}} + \Delta\mu_i$, where μ_i^{elem} is the chemical potential of element i in its standard phase, referenced to the total energy of the elementary phases at zero Kelvin [i.e., O$_2(g)$ and Cu(s)].

The allowed values of $\Delta\mu_i$ are determined from a set of thermodynamic limits. The upper limit is $\Delta\mu_i \leqslant 0$ where element i precipitates to its standard state, in this case metallic copper and molecular oxygen in the gas phase. Also, to avoid the formation of secondary solids, i.e., Cu$_4$O$_3$ and CuO, the chemical potentials must also be bound by

$$4\Delta\mu_{\mathrm{Cu}} + 3\Delta\mu_{\mathrm{O}} \leqslant \Delta H_{\mathrm{f}}(\mathrm{Cu_4O_3}), \quad (2)$$

$$\Delta\mu_{\mathrm{Cu}} + \Delta\mu_{\mathrm{O}} \leqslant \Delta H_{\mathrm{f}}(\mathrm{CuO}). \quad (3)$$

Finally, to maintain the thermodynamic equilibrium with Cu$_2$O, the chemical potentials $\Delta\mu_{\mathrm{Cu}}$ and $\Delta\mu_{\mathrm{O}}$ are constrained by the equilibrium condition

$$2\Delta\mu_{\mathrm{Cu}} + \Delta\mu_{\mathrm{O}} = \Delta H_{\mathrm{f}}(\mathrm{Cu_2O}). \quad (4)$$

The total energies of the phases competing with Cu$_2$O, i.e., Cu$_4$O$_3$ and CuO, were calculated using their respective unit cells. For tetragonal Cu$_4$O$_3$, a primitive cell containing 14 atoms was used together with the antiferromagnetic spin ordering leading to the observed lowest energy configuration [61–63]. For monoclinic CuO, the experimentally observed antiferromagnetically ordered unit cell with 16 atoms was used [64,65].
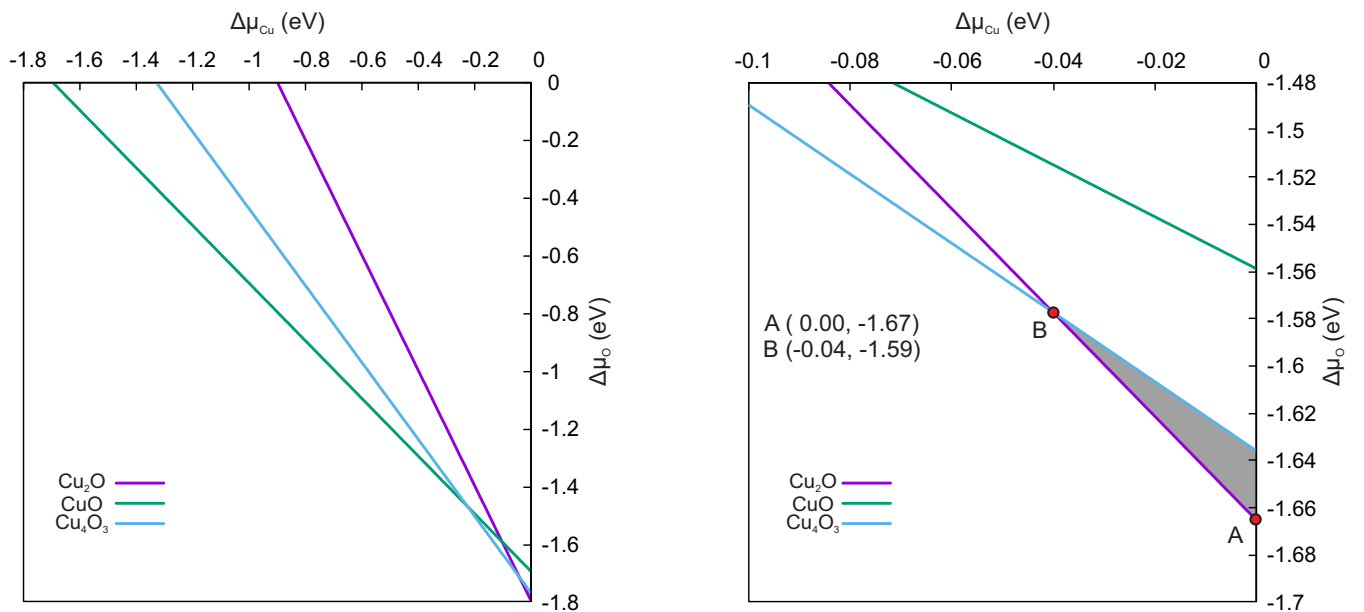

FIG. 2. Phase stability in the range of accessible chemical potentials for Cu$_2$O with the figure on the left indicating the whole range and the figure on the right showing a magnification of the region of interest. Limits are imposed by the formation of competing phases.

TABLE II. Structural distortion, dopant-anion bond distance and bond distance distortion (with respect to the pristine Cu-O bond distance of 1.831 Å).

	Sc	Ti	V	Cr	Mn	Fe	Co	Ni	Zn
Lattice Distortion (%)	0.731	0.714	0.505	0.363	0.442	0.272	0.155	0.078	0.349
d(TM-O) (Å)	1.981	2.067	1.909	1.987	1.939	1.861	1.832	1.891	1.828
Δd(TM-O) (%)	8.158	12.836	4.246	8.452	5.850	1.600	0.034	3.256	−0.184

III. RESULTS AND DISCUSSION

A. Formation enthalpies of pristine Cu_2O

Calculated formation enthalpies of Cu_2O, Cu_4O_3, and CuO are reported in Table I. Qualitatively, both $DFT + U$ and HSE06 predict Cu_2O to be more stable than CuO and give energies very close to experimental trends (differences most likely arise from temperature effects when comparing with tabulated values). From the obtained formation enthalpies and constraints set by Eqs. (2)–(4), boundaries for the chemical potential can be calculated, which are shown in Fig. 2. The chemical potentials for Cu (points A and B in Fig. 2, right), providing boundary values for cation substitution energies, possess values in a very narrow range. Hence, we explicitly consider only point A, with chemical potential values of $\Delta\mu_{Cu} = 0$ eV and $\Delta\mu_O = -1.67$ eV. This approach illustrates the importance of taking competing phases into account, as otherwise calculated defect energetics can end up describing unphysical conditions [66,67].

B. Single substitutional cation-doped Cu_2O

First row transition metal (FRTM) atoms have been introduced into Cu_2O by substitution of Cu on the copper site. The cubic Cu_2O structure holds only one nonequivalent copper position, resulting in one unique configuration for the position of the dopant in the supercell. The substitution of one Cu atom with a FRTM does not alter the geometry substantially, giving a maximum distortion of only 0.7% in the lattice parameter for Ti and Sc dopants, compared to the undistorted structure. Complete results are presented in Table II. The calculated TM-O bond distances are increased for all dopant atoms, compared to the Cu-O bond length of the pure host, apart from the Zn dopant, where a small bond shortening was observed, most likely due to the fact that the Zn d orbitals are full. Calculated results compare well with trends observed in previous studies [49,50].

The oxidation state of the TM atom replacing a copper atom in Cu_2O remains 1+, maintaining charge balance (charge neutrality) in the material. The stability of doped systems is determined by their defect formation energies,

which are summarized in Table III. For the evaluated range of accessible chemical potentials, all the considered neutral TM defects replacing one copper atom are likely to form. Most favorable formation energies are assigned to Cr and Mn, likely due to the half-filled 3d states resulting in less repulsion between atoms. From the selected dopants, Zn exhibits the highest defect formation energy of 0.888 eV, yet still comparable to intrinsic vacancy formation energies in Cu_2O which range from $0.39-0.97$ eV [69].

The computed unfolded electronic band structure together with the total and TM dopant-projected densities of state of the doped systems are shown in Figs. 3 and 4. The band structure of pristine Cu_2O is altered by the introduction of a FRTM substitutional dopant. When doped with an impurity having a higher atomic number, i.e., Zn replacing Cu, the system gains an excess electron. The Zn dopant introduces a singly occupied impurity level that lies at about 1.387 eV above the valence-band maximum (VBM) and 0.520 eV below the conduction-band minimum (CBM) at the Γ point. Since the impurity level is occupied, the donor atom is neutral. The spin density shows delocalization of the excess electron over the dopant and its neighboring atoms, as shown in Fig. 5. A small magnetization of $0.163\,\mu_B$ was found on the Zn atoms, accompanied by $0.056\,\mu_B$ on the nearest O atom (Table III).

In contrast, when doped with an impurity with a lower atomic number, the system gains a spare hole. Substituting Ni for Cu creates an acceptor impurity level in the spin minority channel. This unoccupied level, which consists of hybridizing Cu and Ni 3d t_{2g} states, lies at $\sim$0.059 eV below the CBM (or $\sim$0.456 eV from the spin minority channel, read from the complementary densities of state), as shown in Figure 3. The spin density is localized on the Ni atom, with a magnetic moment of $0.814\,\mu_B$ on the Ni and a negligible moment of $0.015\,\mu_B$ on the O atom (Figure 5).

A single Co dopant creates a donor level located at 0.536 eV above the VBM in the minority spin channel at the Γ point. The unpaired electron is shared between Co and Cu 3d states, whereas the empty Co 3d states are merged with the Cu_2O conduction band. Fe introduces two occupied donor levels in the spin minority channel, located at 0.480 and 0.888 eV above the VBM, respectively. One additional acceptor

TABLE III. Formation energies for substitutional defects on the copper site in Cu_2O together with the accompanying magnetic moment on the transition metal dopant and nearest-neighboring oxygen.

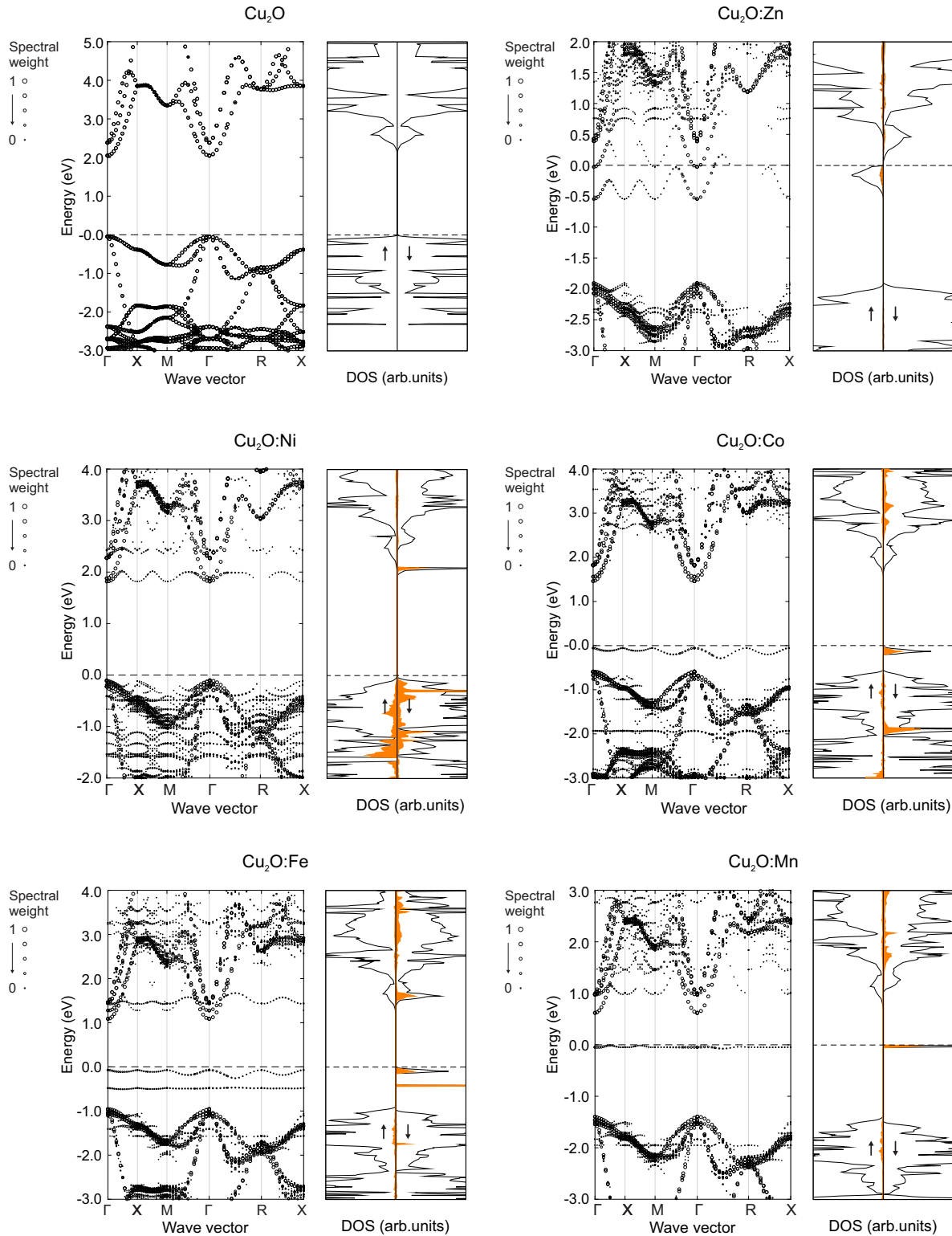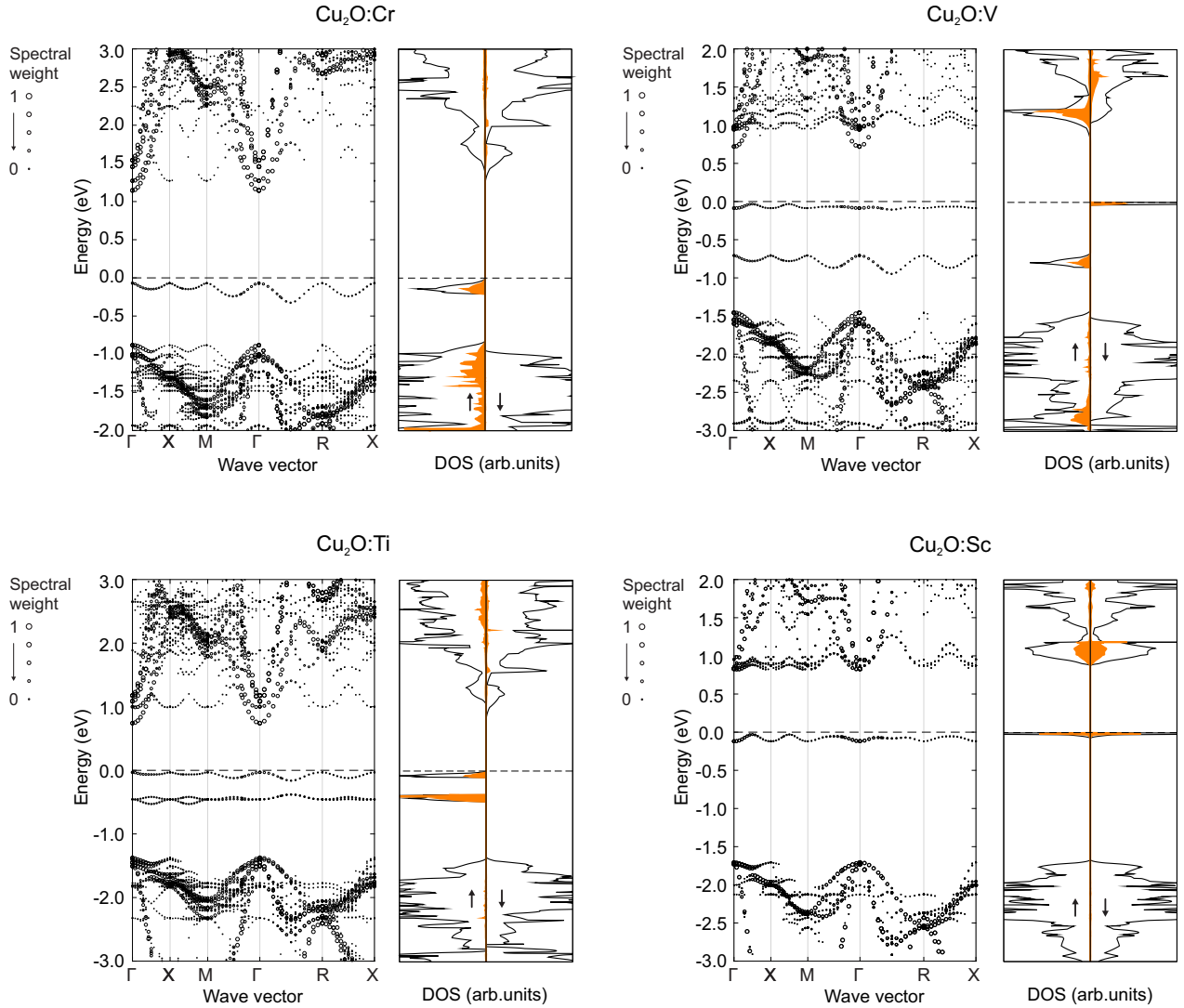|	Sc	Ti	V	Cr	Mn	Fe	Co	Ni	Zn
ΔH_f(eV)	−1.528	−0.807	−0.657	−0.715	−1.448	0.261	−0.408	−0.196	0.888
$m_{TM}(\mu_B)$	0.000	2.025	2.109	4.259	4.252	3.156	2.058	0.814	0.163
$m_O(\mu_B)$	0.000	0.109	0.013	0.074	0.035	0.033	0.023	0.015	0.056

FIG. 3. Electronic band structures together with total (black line) and TM dopant-projected densities of state (orange line) of clean and doped Cu$_2$O. Top left figure shows the undoped Cu$_2$O supercell after performing unfolding of the bands. The dashed line indicates the highest occupied state and arrows represent different spin channels.

level can be identified at approximately 0.350 eV above the CBM.

A single impurity band is created when Cu is replaced by Mn or Cr. Substitutional Mn creates an intermediate impurity level located at around 1.351 eV above the VBM in the spin minority channel, whereas Cr induces an intermediate level in the spin majority channel at around 0.817 eV above the VBM. The empty 3d states are merged with the conduction band

FIG. 4. Electronic band structures together with total (black line) and TM dopant-projected densities of state (orange line) of doped Cu_2O. The dashed line indicates the highest occupied state and arrows represent different spin channels.

for Mn doping, while in the case of Cr doping the filled $3d$ states are placed slightly below the valence band. Mn and Cr also shown strong magnetization of 4.252 μ_B and 4.259 μ_B, respectively, on the impurity dopant atom.

A single substitutional V dopant atom creates two donor states within the band gap of Cu_2O. The first one is located at about 0.842 eV above the VBM, whilst the second is found at 1.370 eV above the VBM.

One doubly-occupied donor band at 0.917 eV from the VBM and one single occupied donor impurity band located at 1.342 eV from the VBM can be identified when a single Ti atoms replaces Cu in Cu_2O. The introduction of a Sc dopant creates an intermediate band level occupied in both spin channels at around 1.607 eV from the VBM.

C. Copper vacancies in cation-doped Cu₂O

The situations described above refer to an ideal, perfect crystal where no other defects are present beyond the dopants. In reality, intrinsic Cu vacancies (V_{Cu}) are usually present in

Cu_2O, which could alter the charge state of the TM dopant. To explore the stabilization of the electronic structure and simulate conditions closer to experiments, one additional V_{Cu} is introduced in the previously doped system. The complementing band structure has been omitted from this analysis due to increased computational cost. Clustering effects were noted when the V_{Cu} was introduced in the proximity of the extrinsic dopant, demonstrating lower formation energies (not shown), as has been observed in previous studies [14,49,70].

The additional hole generated by the V_{Cu} compensates the electron donation effect induced by the single Zn dopant. In the presence of the copper vacancy, the defect formation energy is lowered by 0.493 eV, while the donor level and the magnetization are fully quenched (values listed in Table IV). Empty Zn $4s$ states are hybridized with the Cu_2O conduction band with an overall band gap calculated from single particle levels to be 1.909 eV, as shown in Fig. 6. In contrast, the additional V_{Cu} together with the Ni dopant increases the defect formation energy by 0.946 eV. The additional hole is now transferred to the Ni impurity, creating two empty states in the
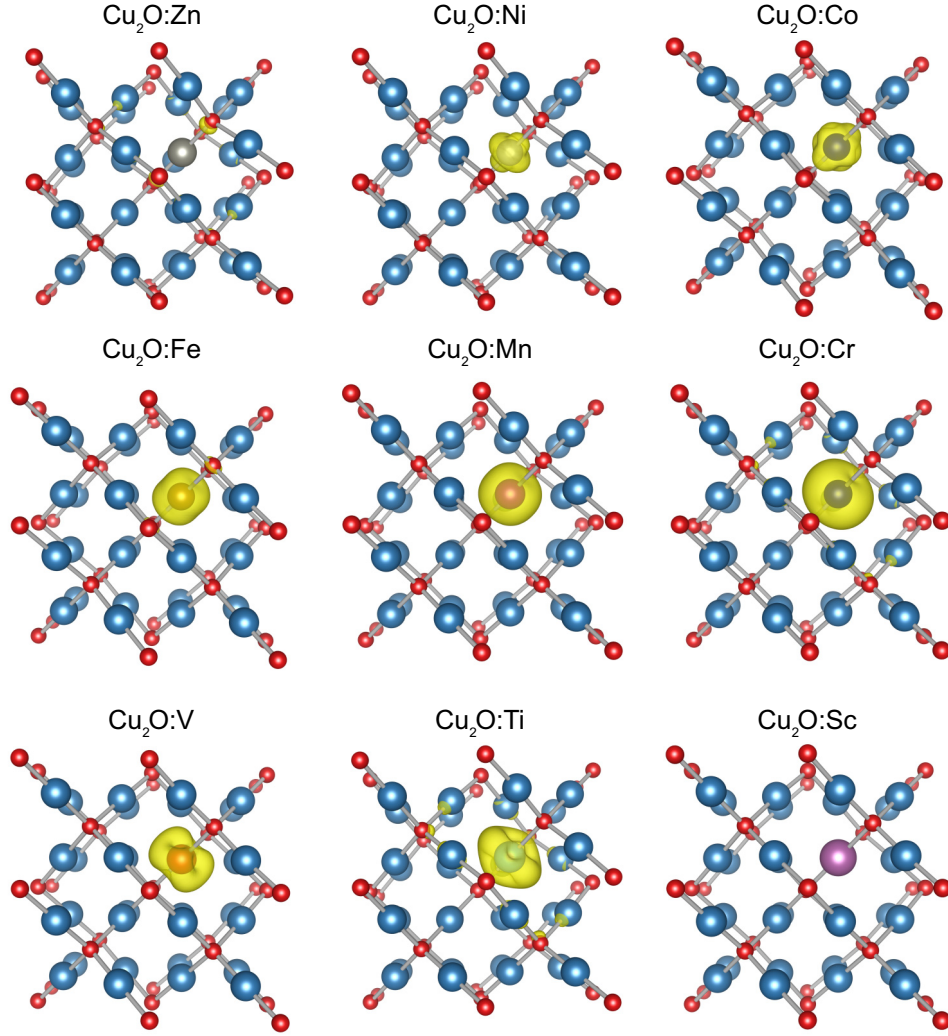
FIG. 5. Spin density difference (depicted in yellow) for TM doped Cu$_2$O. Isosurface level set to 0.011 e/Å2. Red and blue spheres represent oxygen and copper atoms, respectively, while the differently colored atoms represent the transition metal dopant.

minority spin channel, located at 0.866 and 1.532 eV above the VBM, respectively. The magnetization on the Ni impurity atom is increased to 1.502 μ_B, arising from rearranged unpaired electrons of Ni d states.

A V$_{Cu}$ located near the Co dopant features an increase in the formation energy, creating empty states within the conduction band. One additional singly unoccupied state in the spin minority channel originating from Co 3d and 4s orbitals is located around 1.260 eV above the VBM. For the systems doped with Fe, Mn, Cr, and V, a lowering of the defect formation energy is observed. In contrast to the system

without an additional Cu vacancy, empty states within the gap are created. Their positions relative to the CBM minority spin channel are 0.640 and 0.260 eV for Fe and Mn, respectively. The Cr dopant creates two acceptor states within the gap, one positioned at 1.352 eV and the other at 2.245 eV above the VBM. Substitution by V favors an electron transfer from the V 3d band, where the formed acceptor level becomes merged with the bottom of the CBM. The net magnetization per impurity atom is increased for the Fe-, Mn-, Cr- and V-doped system in the material with the V$_{Cu}$ due to increased number of spin unpaired electrons.

TABLE IV. Formation energies for substitutional defects on the copper site with an additional copper vacancy in Cu$_2$O together with the accompanying magnetic moment on the transition metal dopant and nearest-neighboring oxygen.

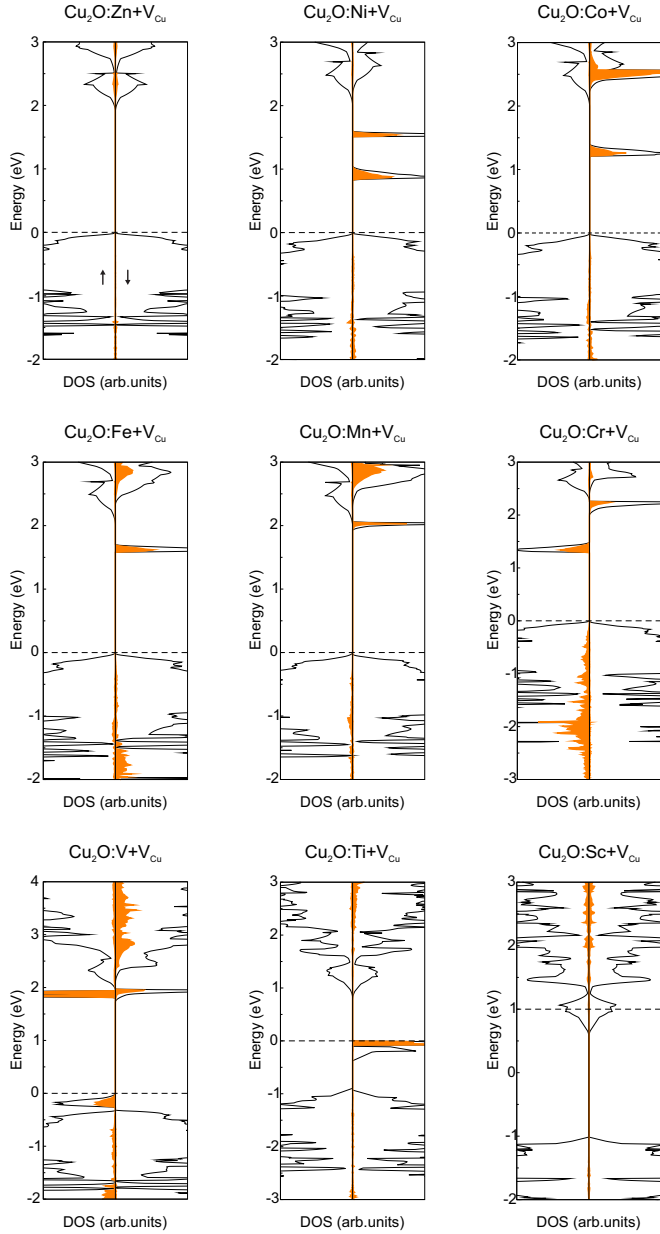| TM + V$_{Cu}$	Sc	Ti	V	Cr	Mn	Fe	Co	Ni	Zn
ΔH_f(eV)	−1.931	0.004	−0.799	−0.139	−1.540	−0.114	0.172	0.750	0.398
m$_{TM}$(μ_B)	0.000	1.768	2.575	3.803	4.546	3.541	2.507	1.502	0.000
m$_O$(μ_B)	0.000	0.017	0.048	0.045	0.034	0.047	0.041	0.039	0.000

FIG. 6. Total (black line) and TM dopant-projected (orange line) densities of state of TM doped Cu_2O with one additional Cu vacancy. The dashed line indicated the highest occupied state and arrows represent different spin channels.

The Ti- and Sc-doped Cu_2O systems undergo substantial lattice distortions. The impurity atoms move into the tetrahedral position, increasing the formation energy by 0.811 eV for Ti and lowering it by 0.393 eV for Sc. The Sc-doped system is found to be metallic in nature, due to hybridized Cu $3d$, $4s$, and O $2p$ states crossing the Fermi level.

Results shown in Table V illustrate the Bader charge distribution analysis undertaken on the extrinsic dopant and its nearest neighboring atoms. Charge differences confirm the increased loss of negative charge (i.e., positive charge gain—increased hole concentration) on the transition metal dopant between the systems without and with the additional copper vacancy. This hole localization is further highlighted by visualizing the spin density difference, as shown in Fig. 7. Small charge fluctuations are observed on the nearest neighboring Cu atoms, surrounding the dopant, with a value between 0.01 and 0.03 e^-. The charges on the nearest neighboring oxygen atoms in the stoichiometric FRTM-doped systems are distributed symmetrically, in contrast to the FRTM-doped system with the additional copper vacancy. The copper vacancy leads to a distortion of the TM-oxygen distances causing slight increases in the bond lengths and, as a consequence, fluctuation of the charge.

Partial charge density for the vacant impurity bands, created when Cu_2O was doped with TM and one additional copper vacancy, have been presented in Fig. 8. Shown are systems where a distinct impurity band was observed, leaving out Zn and Sc due to merging of states with the CBM. Delocalization of the additionally created states is observed in the case of Ni and Co, whilst the remaining systems demonstrate a high degree of localization of states on the impurity atom. Delocalized states do not act as hole traps, thus leading to potentially favorable increases in conductivity [18].

Electronic structure calculations provide insight into charge transfer processes, occurrence of additional impurity states within the host's band gap or the degree of localization of excess carriers. However, direct impact on photovoltaic properties of relevance is often difficult to assess. One available metric to do so is the so-called spectroscopic maximum limited efficiency (SLME) approach, developed by Yu and Zunger [71]. It extends beyond the commonly used Shockley-Queisser criterion to incorporate a fraction of nonradiative recombination, whilst approximating the power conversion efficiency (PCE) of a material employed as a thin film absorber.

The calculated SLME for substitutionally doped Cu_2O without and with an additional copper vacancy are shown in

TABLE V. Bader charge analysis of first row transition metal doped Cu_2O without and with an additional copper vacancy in the vicinity of the dopant atom. Values listed are in e^-. NN represents the nearest neighbor and NNN the next nearest neighbor to the dopant atom.

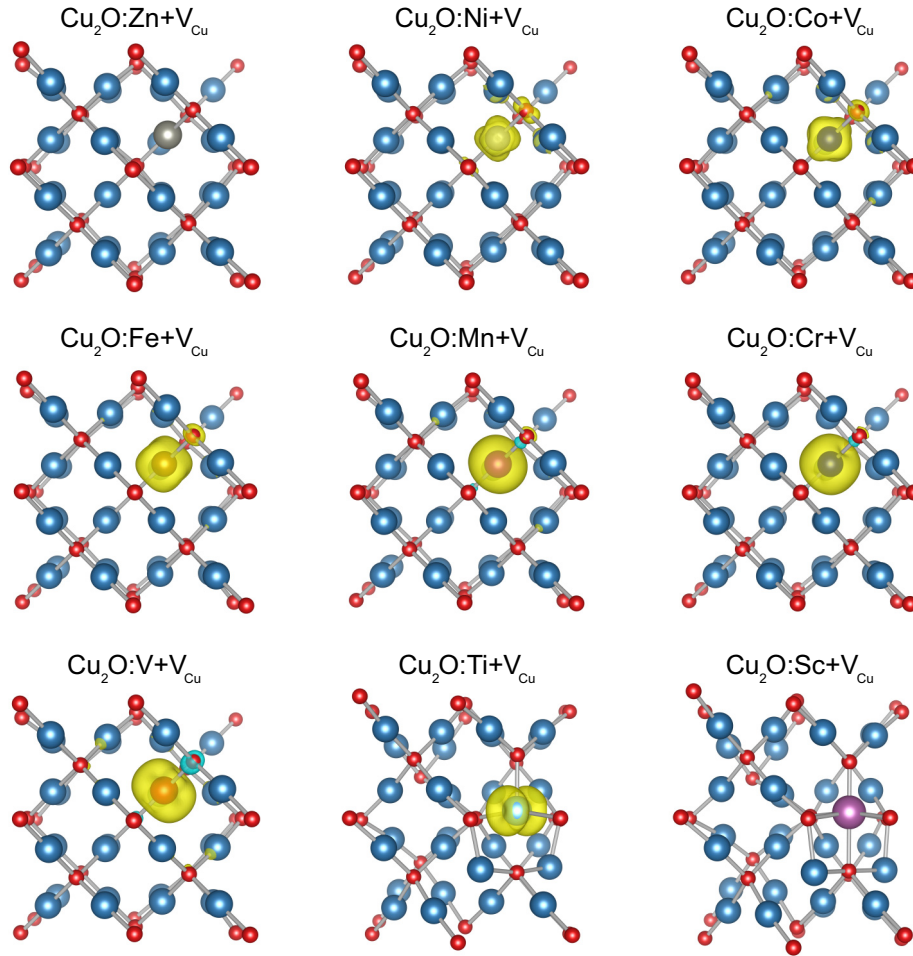|	Sc	Ti	V	Cr	Mn	Fe	Co	Ni	Zn
TM_{Cu}	+1.585	+1.150	+1.118	+0.877	+0.914	+0.759	+0.633	+0.522	+0.939
$TM_{Cu} + V_{Cu}$	+1.879	+1.544	+1.223	+1.188	+1.201	+1.090	+0.980	+0.909	+1.084
O_{NN} (TM_{Cu})	−1.232	−1.215	−1.199	−1.232	−1.145	−1.158	−1.134	−1.129	−1.160
O_{NN} ($TM_{Cu} + V_{Cu}$)	−1.150	−1.160	−1.106	−1.060	−1.066	−1.069	−1.066	−1.066	−1.069
	−1.121	−1.196	−1.108	−1.125	−1.122	−1.120	−1.092	−1.082	−1.110
Cu_{NN}	+0.532	+0.560	+0.536	+0.570	+0.531	+0.567	+0.563	+0.549	+0.598
$Cu_{NN} + V_{Cu}$	+0.568	+0.574	+0.555	+0.555	+0.546	+0.556	+0.588	+0.546	+0.548

FIG. 7. Spin density difference (depicted in yellow) for TM doped Cu$_2$O with an additional V$_{Cu}$. Isosurface level set to $0.011\,e/\text{Å}^2$. Red and blue spheres represent oxygen and copper atoms, respectively, while the differently colored atoms represent the transition metal dopant.

Figs. 9 and 10, respectively. The most prominent enhanced effect is observed for Zn and Ni, when considering single substitutional defects on the copper site in Cu$_2$O, whereas Mn, V, and Ti impaired the already low efficiency of pure Cu$_2$O (efficiencies lowering those of pristine Cu$_2$O were omitted from the graph). The introduction of an additional copper vacancy stabilizes the system energetically, in addition to favoring higher light absorption. The main cause of the significant increase in SLME is attributed to the nature of interband transitions between the VBM and CBM. Pure Cu$_2$O exhibits a parity forbidden lowest fundamental absorption transition (neglecting excitons), hindering immediate light capturing until $\sim$2.6 eV. In the case of doped Cu$_2$O, defects create band levels within the band gap, allowing an earlier absorption onset. This can be observed in the calculated absorption coefficients (Figs. 9 and 10), which indicate the absorption probability of incident photons of different energies. In both types of studied defect systems, a shift of the absorption onset towards lower energies is observed, approaching the ideal band-gap value for photovoltaic materials which lies around $1.3-1.5$ eV [72,73]. Since SLME incorporates the difference between the first direct allowed interband transition and the fundamental

band gap to estimate nonradiative recombination processes, the resulting efficiencies are observed to have increased.

While interpreting these results, one has to keep in mind the theoretical limitations of the employed methodology. Spin-orbit coupling and excitonic effects, which could influence the calculated electronic structure, were omitted from this study due to their significant increased computational cost. Furthermore, defect properties (i.e., mobility, arrangement, migration) are significantly influenced by temperature fluctuations, which are not accessible within the methodological framework used here. In addition, values illustrated within this work are valid for a single-crystal material, where band alignment or interface barrier effects, though valid in real-time applications, are not present. Despite those limitations and their most likely negative effect on the calculated absorption efficiencies, the results discussed here match experimentally observed phenomena. A threefold improvement was shown in the overall PCE of Cu$_2$O thin films doped with Zn compared to clean p-type Cu$_2$O ones [17], confirming the theoretical calculated values. In addition, Fe-doped Cu$_2$O films have shown significant improvement of optical transmittance over undoped samples [29].
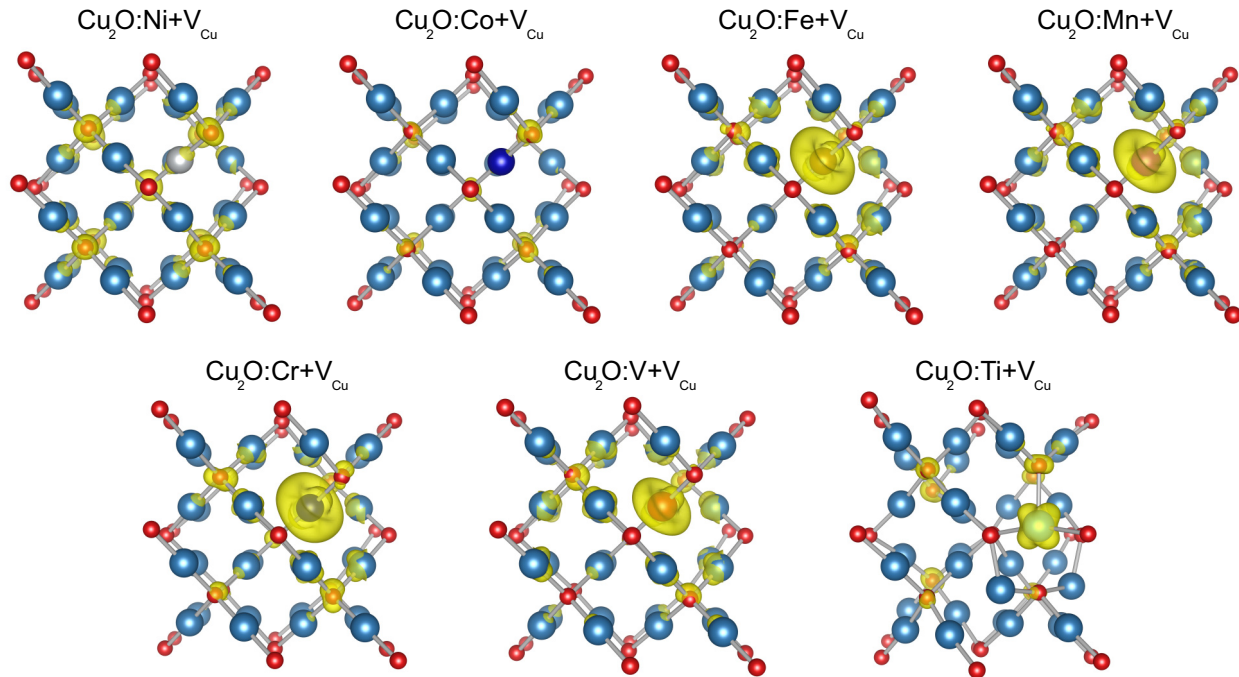
FIG. 8. Partial charge density (depicted in yellow) representation of vacant impurity band in the electronic structure of TM doped Cu_2O with one additional copper vacancy on the nearest-neighboring site. Isosurface level set to $0.03\,e/\text{Å}^2$. Red and blue spheres represent oxygen and copper atoms, respectively, while the differently colored atoms represent the transition metal dopant.
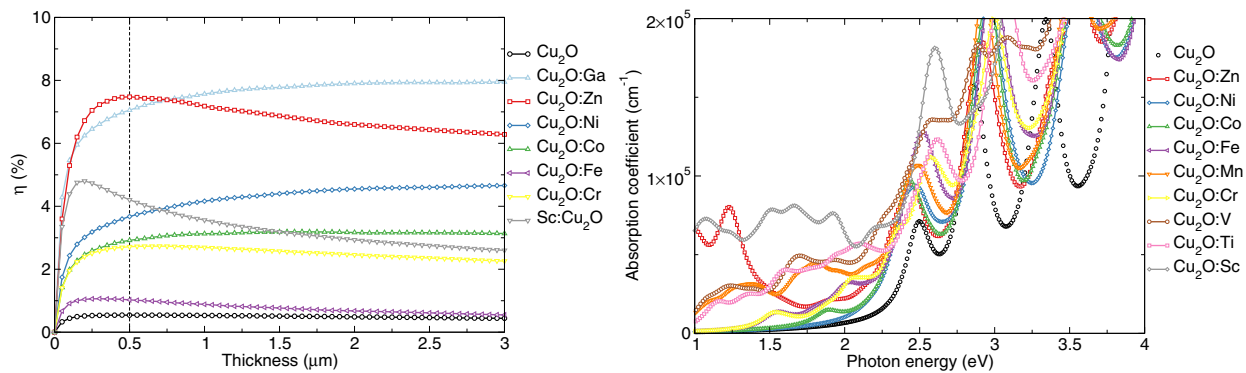

FIG. 9. Calculated SLME (left) together with the absorption coefficient (right) together for FRTM substitutional dopants in Cu_2O. SLME values lower than the initial Cu_2O (denoted with the black line) were omitted from the graph.
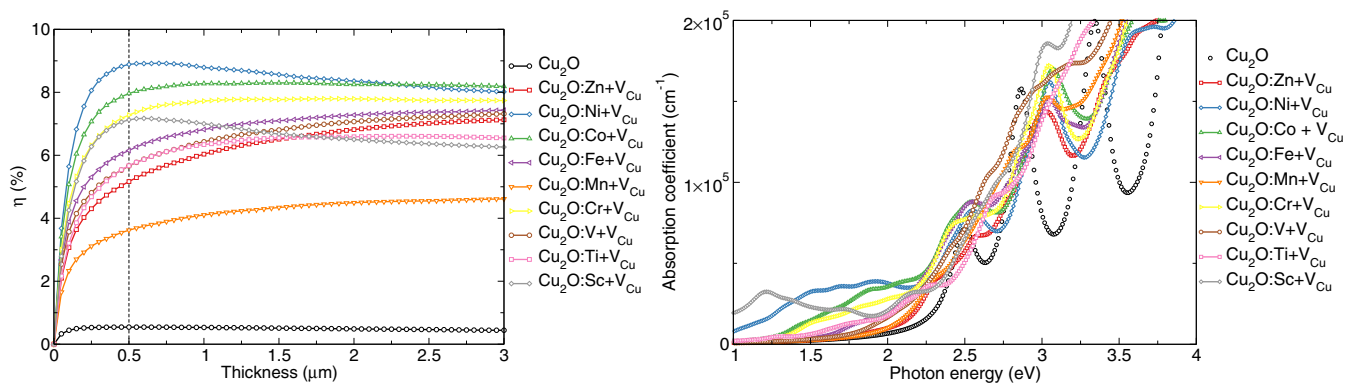

FIG. 10. Calculated SLME (right) together with the absorption coefficient (left) for FRTM substitutional dopants in Cu_2O with an additional copper vacancy. Values for SLME lower than the one for pristine Cu_2O (denoted with the black line) were omitted from the graph.

IV. CONCLUSION

We have carried out a systematic computational study within a hybrid DFT formalism of the electronic and optical properties of transition metal-doped Cu_2O. Additional copper vacancies, observed intrinsically in Cu_2O, were also considered, and were found to have a stabilizing effect on the defect formation energies. The effect of dopants on the pristine band structure of Cu_2O was analysed, identifying beneficial change from shallow impurity levels to deep intermediate states as additional copper vacancies are introduced in the system. To assess the overall absorption potential of doped compounds, the SLME metric was calculated. A positive effect on the overall photovoltaic conversion efficiency was observed for a majority of dopants, where Ni, Fe, and Zn reveal the most promising effect. Results presented in this work indicate the potential of first row transition metals as favorable dopants for improved absorption properties of Cu_2O.

[1] A. Martinez-Ruiz, M. G. Moreno, and N Takeuchi, First principles calculations of the electronic properties of bulk Cu_2O, clean and doped with Ag, Ni, and Zn, Solid State Sci. **5**, 291 (2003).

[2] S. K. Wallace, D. B. Mitzi, and A Walsh, The steady rise of kesterite solar cells, ACS Energy Lett. **2**, 776 (2017).

[3] R. E Brandt *et al.*, Searching for "defect-tolerant" photovoltaic materials: Combined theoretical and experimental screening, Chem. Mater. Accepted **29**, 4667 (2017).

[4] A. Jain, Y. Shin, and K. A Persson, Computational predictions of energy materials using density functional theory, Nat. Rev. Mater. **1**, 15004 (2016).

[5] S. Chatterjee, S. K. Saha, and A. J. Pal, Formation of all-oxide solar cells in atmospheric condition based on Cu_2O thin-films grown through SILAR technique, Sol. Energy Mater. Sol. Cells **147**, 17 (2016).

[6] Q. Huang, J. Li, and X Bi, The improvement of hole transport property and optical band gap for amorphous Cu_2O films, J. Alloys Compd. **647**, 585 (2015).

[7] S. S Wilson *et al.*, Interface stoichiometry control to improve device voltage and modify band alignment in ZnO/Cu_2O heterojunction solar cells, Energy Environ. Sci. **7**, 3606 (2014).

[8] R. Wick and S. D Tilley, Photovoltaic and photoelectrochemical solar energy conversion with Cu_2O, J. Phys. Chem. C **119**, 26243 (2015).

[9] N. Zhang, J. Sun, and H. Gong, Transparent *p*-type semiconductors: Copper-based oxides and oxychalcogenides, Coatings **9**, 137 (2019).

[10] J. Linnera and A. J. Karttunen, *Ab initio* study of the lattice thermal conductivity of Cu_2O using the generalized gradient approximation and hybrid density functional methods, Phys. Rev. B **96**, 014304 (2017).

[11] M. Giar, M. Heinemann, and C. Heiliger, Phonon properties of copper oxide phases from first principles, Phys. Rev. B **96**, 075202 (2017).

[12] S. Lany, Band-structure calculations for the 3*d* transition metal oxides in *GW*, Phys. Rev. B **87**, 085112 (2013).

[13] T Ha *et al.*, Single-crystalline Cu_2O thin films of optical quality as obtained by the oxidation of single-crystal Cu thin films at low temperature, APL Mater. **7**, 031115 (2019).

[14] L. Y. Isseroff and E. A. Carter, Electronic structure of pure and doped cuprous oxide with copper vacancies: Suppression of trap states, Chem. Mater. **25**, 253 (2013).

[15] L. Y. Isseroff and E. A. Carter, Importance of reference Hamiltonians containing exact exchange for accurate one-shot GW calculations of Cu_2O, Phys. Rev. B **85**, 235142 (2012).

[16] B. K Meyer *et al.*, Binary copper oxide semiconductors: From materials towards devices, Phys. Status Solidi **249**, 1487 (2012).

[17] C. Zhu and M. J. Panzer, Synthesis of $Zn:Cu_2O$ thin films using a single step electrodeposition for photovoltaic applications, ACS Appl. Mater. Interfaces **7**, 5624 (2015).

[18] M. D. McCluskey and E. E. Haller, *Dopants and Defects in Semiconductors* (CRC Press, Boca-Raton, 2012).

[19] F. Hu, Y. Zou, L. Wang, Y. Wen, and Y. Xiong, Photostable Cu_2O photoelectrodes fabricated by facile Zn-doping electrodeposition, Int. J. Hydrogen Energy **41**, 15172 (2016).

[20] O. Porat and I. Riess, Defect chemistry of $Cu_{2-y}O$ at elevated temperatures. Part I: Non-stoichiometry, phase width and dominant point defects, Solid State Ionics **74**, 229 (1994).

[21] O. Porat and I. Riess, Defect chemistry of $Cu_{2-y}O$ at elevated temperatures. Part II: Electrical conductivity, thermoelectric power and charged point defects, Solid State Ionics **81**, 29 (1995).

[22] G. K. Paul, Y. Nawa, H. Sato, T. Sakurai, and K. Akimoto, Defects in Cu_2O studied by deep level transient spectroscopy, Appl. Phys. Lett. **88**, 141901 (2006).

[23] D. O. Scanlon, B. J. Morgan, G. W. Watson, and A. Walsh, Acceptor Levels in *p*-Type Cu_2O: Rationalizing Theory and Experiment, Phys. Rev. Lett. **103**, 096405 (2009).

[24] M. Nolan and S. D. Elliott, Tuning the electronic structure of the transparent conducting oxide Cu_2O, Thin Solid Films **516**, 1468 (2008).

[25] D. O. Scanlon and G. W. Watson, Undoped n-type CuO: Fact or fiction? J. Phys. Chem. Lett. **1**, 2582 (2010).

[26] K Akimoto *et al.*, Thin film deposition of Cu_2O and application for solar cells, Sol. Energy **80**, 715 (2006).

[27] L. Zhang, L. McMillon, and J. McNatt, Gas-dependent bandgap and electrical conductivity of Cu_2O thin films, Sol. Energy Mater. Sol. Cells **108**, 230 (2013).

[28] F. Biccari, C. Malerba, and A. Mittiga, Impurity effects in Cu_2O (2013), arXiv:1310.5341.

[29] S Satheeskumar *et al.*, Enhancing the structural, optical and magnetic properties of Cu_2O films deposited using a SILAR technique through Fe-doping, J. Mater. Sci. Mater. Electron. **29**, 9354 (2018).

[30] K Kardarian *et al.*, Effect of Mg doping on Cu_2O thin films and their behavior on the TiO_2/Cu_2O heterojunction solar cells, Sol. Energy Mater. Sol. Cells **147**, 27 (2016).

[31] S. N Kale *et al.*, Magnetism in cobalt-doped Cu_2O thin films without and with Al, V, or Zn codopants, Appl. Phys. Lett. **82**, 2100 (2003).

[32] I. S Brandt *et al.*, Enhanced defect-mediated ferromagnetism in Cu_2O by Co doping, J. Magn. Magn. Mater. **441**, 374 (2017).

[33] G. S Chang *et al.*, Defect-induced ferromagnetism in Mn-doped Cu_2O, J. Phys. Condens. Matter **20**, 215216 (2008).

[34] F Ye *et al.*, The electrical and thermoelectric properties of Zn-doped cuprous oxide, Thin Solid Films **603**, 395 (2016).

[35] E. Albanese, M. Leccese, C. Di Valentin, and G. Pacchioni, Magnetic properties of nitrogen-doped ZrO_2: Theoretical evidence of absence of room temperature ferromagnetism, Sci. Rep. **6**, 31435 (2016).

[36] G. Kresse and D. Joubert, From ultrasoft pseudopotentials to the projector augmented-wave method, Phys. Rev. B **59**, 1758 (1999).

[37] P. E. Blöchl, Projector augmented-wave method, Phys. Rev. B **50**, 17953 (1994).

[38] J. Perdew, K. P. Burke, and M Ernzerhof, Generalized Gradient Approximation Made Simple. Phys. Rev. Lett. **77**, 3865 (1996).

[39] S. L. Dudarev, G. A. Botton, S. Y. Savrasov, C. J. Humphreys, and A. P. Sutton, Electron-energy-loss spectra and the structural stability of nickel oxide: An LSDA+U study, Phys. Rev. B **57**, 1505 (1998).

[40] Z. Xu, Y. V. Joshi, S. Raman, and J. R. Kitchin, Accurate electronic and chemical properties of 3d transition metal oxides using a calculated linear response U and a DFT + U (V) method, J. Chem. Phys. **142**, 144701 (2015).

[41] E. Assmann *et al.*, Oxide Heterostructures for Efficient Solar Cells, Phys. Rev. Lett. **110**, 078701 (2013).

[42] C. H. Chien, S. H. Chiou, G. Y. Guo, and Y. Der Yao, Electronic structure and magnetic moments of 3d transition metal-doped ZnO, J. Magn. Magn. Mater. **282**, 275 (2004).

[43] J. Heyd, G. E. Scuseria, and M. Ernzerhof, Hybrid functionals based on a screened Coulomb potential, J. Chem. Phys. **118**, 8207 (2003).

[44] J. Heyd and G. E. Scuseria, Efficient hybrid density functional calculations in solids: Assessment of the Heyd-Scuseria-Ernzerhof screened Coulomb hybrid functional, J. Chem. Phys. **121**, 1187 (2004).

[45] J. Heyd, G. E. Scuseria, and M. Ernzerhof, Erratum: "Hybrid functionals based on a screened Coulomb potential" [J. Chem. Phys. **118**, 8207 (2003)], J. Chem. Phys. **124**, 219906(E) (2006).

[46] M. Gajdoš, K. Hummer, G. Kresse, J. Furthmüller, and F. Bechstedt, Linear optical properties in the projector-augmented wave methodology, Phys. Rev. B **73**, 045112 (2006).

[47] S. Grimme, J. Antony, S. Ehrlich, and H. Krieg, A consistent and accurate *ab initio* parametrization of density functional dispersion correction (DFT-D) for the 94 elements H-Pu, J. Chem. Phys. **132**, 154104 (2010).

[48] Y Wang *et al.*, Transmittance enhancement and optical bandgap widening of Cu_2O thin films after air annealing, J., Appl. Phys. **115**, 073505 (2014).

[49] M. Sieberer, J. Redinger, and P. Mohn, Electronic and magnetic structure of cuprous oxide Cu_2O doped with Mn, Fe, Co, and Ni: A density-functional theory study, Phys. Rev. B **75**, 035203 (2007).

[50] A. Soon, J. Wallman, B. Delley, and C. Stampfl, Early transition metal dopants in cuprous oxide: To spin or not to spin, Curr. Appl. Phys. **13**, 1707 (2013).

[51] H. J. Monkhorst and J. D. Pack, Special points for Brillouin-zone integrations, Phys. Rev. B **13**, 5188 (1976).

[52] D. O. Scanlon, B. J. Morgan, and G. W. Watson, Modeling the polaronic nature of p-type defects in Cu_2O: The failure of GGA and GGA + U. J. Chem. Phys. **131**, 124703 (2009).

[53] J. Buckeridge, D. O. Scanlon, A. Walsh, and C. R. A. Catlow, Automated procedure to determine the thermodynamic stability of a material and the range of chemical potentials necessary for its formation relative to competing phases and compounds, Comput. Phys. Commun. **185**, 330 (2014).

[54] M. Yu and D. R. Trinkle, Accurate and efficient algorithm for Bader charge integration, J. Chem. Phys. **134**, 064111 (2011).

[55] W. Tang, E. Sanville, and G Henkelman, A grid-based Bader analysis algorithm without lattice bias, J. Phys. Condens. Matter **21**, 084204 (2009).

[56] E. Sanville, S. D. Kenny, R. Smith, and G. Henkelman, Improved grid-based algorithm for Bader charge allocation, J. Comput. Chem. **28**, 899 (2007).

[57] R. Grau-Crespo, S. Hamad, C. R. A. Catlow, and N. H. de Leeuw, Symmetry-adapted configurational modelling of fractional site occupancy in solids, J. Phys. Condens. Matter **19**, 256201 (2007).

[58] K. Momma and F. Izumi, VESTA 3 for three-dimensional visualization of crystal, volumetric and morphology data, J. Appl. Crystallogr. **44**, 1272 (2011).

[59] O. Rubel, A. Bokhanchuk, S. J. Ahmed, and E. Assmann, Unfolding the band structure of disordered solids: From bound states to high-mobility Kane fermions, Phys. Rev. B **90**, 115202 (2014).

[60] V. Popescu and A. Zunger, Effective Band Structure of Random Alloys, Phys. Rev. Lett. **104**, 236403 (2010).

[61] L. Pinsard-Gaudart, J. Rodríguez-Carvajal, A. Gukasov, and P. Monod, Magnetic properties of paramelaconite (Cu_4O_3): A pyrochlore lattice with $S = \frac{1}{2}$, Phys. Rev. B **69**, 104408 (2004).

[62] D. Djurek, M. Prester, D. Drobac, M. Ivanda, and D. Vojta, Magnetic properties of nanoscaled paramelaconite $Cu_4O_{3-x}(x = 0.0$ and $0.5)$, J. Magn. Magn. Mater. **373**, 183 (2015).

[63] J. F. Pierson, E. Duverger, and O. Banakh, Experimental and theoretical contributions to the determination of optical properties of synthetic paramelaconite, J. Solid State Chem. **180**, 968 (2007).

[64] J. B. Forsyth, P. J. Brown, and B. M. Wanklyn, Magnetism in cupric oxide, J. Phys. C Solid State Phys. **21**, 2917 (1988).

[65] T. J. Smart, A. C. Cardiel, F. Wu, K.-S. Choi, and Y. Ping, Mechanistic insights of enhanced spin polaron conduction in CuO through atomic doping, npj Comput. Mater. **4**, 61 (2018).

[66] D. O. Scanlon, J. Buckeridge, C. R. A. Catlow, and G. W. Watson, Understanding doping anomalies in degenerate *p*-type semiconductor LaCuOSe, J. Mater. Chem. C **2**, 3429 (2014).

[67] D. Tahir and S. Tougaard, Electronic and optical properties of Cu, CuO and Cu₂O studied by electron spectroscopy, J. Phys. Condens. Matter **24**, 175002 (2012).

[68] D. R. Lide, *CRC Handbook of Chemistry and Physics, Internet Version* (CRC Press, Boca Raton, Fl, 2005).

[69] L. I. Bendavid and E. A. Carter, First-principles predictions of the structure, stability, and photocatalytic potential of Cu₂O surfaces, J. Phys. Chem. B **117**, 15750 (2013).

[70] H. Raebiger, S. Lany, and A. Zunger, Impurity Clustering and Ferromagnetic Interactions that are not Carrier Induced in Dilute Magnetic Semiconductors: The Case of Cu2O:Co, Phys. Rev. Lett. **99**, 167203 (2007).

[71] L. Yu and A. Zunger, Identification of Potential Photovoltaic Absorbers Based on First-Principles Spectroscopic Screening of Materials, Phys. Rev. Lett. **108**, 068701 (2012).

[72] W. Shockley and H. J. Queisser, Detailed balance limit of efficiency of *p-n* junction solar cells, J. Appl. Phys. **32**, 510 (1961).

[73] F. H Alharbi *et al.*, An efficient descriptor model for designing materials for solar cells, npj Comput. Mater. **1**, 15003 (2015).

[74] A. Živković, A. Roldan, and N. H. de Leeuw, "Tuning the electronic band gap of Cu₂O via transition metal doping for improved photovoltaic applications", http://doi.org/10.17035/d.2019.0081822100 (2019).